NRC Publications Archive
Archives des publications du CNRC

Lock-in amplitude-phase correlations for enhanced imaging and segmentation in stimulated Raman scattering microscopy

Harper, Alexander N.; Boisvert, Jonathan; Grammatikopoulos, Tassos; Stolow, Albert; Pegoraro, Adrian F.

This publication could be one of several versions: author’s original, accepted manuscript or the publisher’s version. / La version de cette publication peut être l’une des suivantes : la version prépublication de l’auteur, la version acceptée du manuscrit ou la version de l’éditeur.
For the publisher’s version, please access the DOI link below./ Pour consulter la version de l’éditeur, utilisez le lien DOI ci-dessous.

Publisher’s version / Version de l'éditeur:
https://doi.org/10.1364/OE.569993
Optics Express, 33, 19, pp. 39406-39425, 2025-09-09

NRC Publications Archive Record / Notice des Archives des publications du CNRC :
https://nrc-publications.canada.ca/eng/view/object/?id=944e08d2-aa3b-43f9-8803-33d9c72c31f4
https://publications-cnrc.canada.ca/fra/voir/objet/?id=944e08d2-aa3b-43f9-8803-33d9c72c31f4

Access and use of this website and the material on it are subject to the Terms and Conditions set forth at
https://nrc-publications.canada.ca/eng/copyright
READ THESE TERMS AND CONDITIONS CAREFULLY BEFORE USING THIS WEBSITE.

L’accès à ce site Web et l’utilisation de son contenu sont assujettis aux conditions présentées dans le site
https://publications-cnrc.canada.ca/fra/droits
LISEZ CES CONDITIONS ATTENTIVEMENT AVANT D’UTILISER CE SITE WEB.

Questions? Contact the NRC Publications Archive team at PublicationsArchive-ArchivesPublications@nrc-cnrc.gc.ca. If you wish to email the authors directly, please see the first page of the publication for their contact information.

Vous avez des questions? Nous pouvons vous aider. Pour communiquer directement avec un auteur, consultez la première page de la revue dans laquelle son article a été publié afin de trouver ses coordonnées. Si vous n’arrivez pas à les repérer, communiquez avec nous à PublicationsArchive-ArchivesPublications@nrc-cnrc.gc.ca.

National Research Council Canada
Conseil national de recherches Canada

Research Article Vol. 33, No. 19 / 22 Sep 2025 / *Optics Express* 39406

Optics EXPRESS

Lock-in amplitude-phase correlations for enhanced imaging and segmentation in stimulated Raman scattering microscopy

ALEXANDER N. HARPER,[1] **JONATHAN BOISVERT,**[2] **TASSOS GRAMMATIKOPOULOS,**[3] **ALBERT STOLOW,**[1,4,5,6,8] **AND ADRIAN F. PEGORARO**[7,9]

[1] *Department of Chemistry and Biomolecular Sciences, University of Ottawa, 10 Marie Curie Pvt, Ottawa, Ontario, K1N 6N5, Canada*
[2] *Digital Technologies Research Centre, National Research Council Canada, 100 Sussex Drive, Ottawa, Ontario, K1N 5A2, Canada*
[3] *SGS Canada Inc., 185 Concession Street, Lakefield, Ontario, L5T 1W8, Canada*
[4] *Department of Physics, University of Ottawa, 150 Louis-Pasteur Pvt, Ottawa, Ontario, K1N 6N5, Canada*
[5] *Quantum and Nanotechnologies Research Centre, National Research Council Canada, 100 Sussex Drive, Ottawa, Ontario, K1N 5A2, Canada*
[6] *Max Planck-uOttawa Centre for Extreme and Quantum Photonics, 25 Templeton St, Ottawa, Ontario, K1N 7N9, Canada*
[7] *Metrology Research Centre, National Research Council Canada, 100 Sussex Drive, Ottawa, Ontario, K1N 5A2, Canada*
[8] *astolow@uottawa.ca*
[9] *adrian.pegoraro@nrc-cnrc.gc.ca*

Abstract: Modulation transfer-based signal recovery methods, such as stimulated Raman scattering (SRS) microscopy, commonly use lock-in amplifier amplitude and phase outputs, with each providing readily accessible yet complementary information. Here we show that 2D amplitude-phase correlations enhance both imaging and segmentation (chemical specificity) in spectral focusing SRS microscopy, exemplified here by the characterization of an economic lithium ore sample. We additionally demonstrate that bilateral filtering applied to 2D amplitude-phase correlations leads to improved edge-preserving imaging.

1. Introduction

Coherent nonlinear optical microscopies comprise several different techniques, some of which generate label-free, chemical-specific contrast [1–5]. With techniques such as harmonic generation or two-photon fluorescence, new colours are generated and therefore the spectral response is used to discriminate the desired signals [6]. With other techniques, such as pump-probe and thermal reflectance microscopy, it is the temporal response of the system which is used to discriminate signals [7–9]. In this sense, Coherent Raman Microscopy (CRM) is often treated like harmonic generation wherein the spectral response is key. However, as discussed here, it can be advantageous to consider CRM as a temporal pump-probe type process. In CRM, typically two lasers - pump and Stokes - are temporally and spatially overlapped in the sample. When their instantaneous frequency difference matches a Raman mode of the sample, a resonant nonlinear interaction occurs. In Coherent Anti-Stokes Raman Scattering (CARS), spectral filtering is used to discriminate the blue-shifted Anti-Stokes signal. In Stimulated Raman Scattering (SRS), modulation and lock-in methods are typically used. Despite its technical implementation as a pump-probe microscopy, the CRM response is usually discussed in terms of spectral response. When the temporal response is considered, it can be used to help discriminate the instantaneous Raman-resonant signals from certain time-delayed non-Raman background signals [10–12].

#569993 https://doi.org/10.1364/OE.569993
Journal © 2025 Received 20 Jun 2025; revised 13 Aug 2025; accepted 15 Aug 2025; published 9 Sep 2025

We emphasize that, beyond the discrimination of Raman-resonant signals, there is merit in understanding and classifying the spectral/temporal responses of different background signals in heterogeneous samples. By considering CRM as simultaneously a Raman-resonant and a pump-probe process, we show here that a fuller characterization of complex material samples emerges.

In SRS microscopy, broad classes of background signals can be discriminated based on their temporal response. Distinguishing SRS signals based on their instantaneous response was demonstrated using picosecond-SRS [11,12]. In Spectral Focusing SRS microscopy [13–17], the time delay between the two chirped input pulses (here, Pump and Stokes) is scanned and the modulation transfer signal is collected via lock-in amplification (LIA). For the photophysical process of SRS, the time delay (i.e. the instantaneous difference frequency) can be mapped onto a Raman shift. However, for the non-Raman (i.e. background) processes, the time delay is better understood from a pump-probe perspective [18,19]. As we demonstrate here, analysis of LIA amplitude and phase correlations within the time series data, particularly in regions where multiple nonlinear optical signals are simultaneously generated, permits their further disentangling. We also introduce an improved single-frame (i.e. single time delay / single Raman shift) analysis based on the use of bilateral filtering. Treating the LIA phase and amplitude data as complementary, we show that edge-preserving filtering techniques can remove non-Raman background signals, reduce noise and improve species identification even in a single frame, resulting in very rapid SRS chemical imaging of complex, heterogeneous samples.

2. Modelling

We introduce in the following a simple simulation model which illustrates the sometimes counter-intuitive effects of overlapping Raman and non-Raman (i.e. background) signals. The simulation parameters were chosen to be illustrative and informative of how signals from differing photophysical processes can mix when using lock-in amplifier detected modulation-transfer techniques. As such, the values of the input parameters were chosen for illustrative and pedagogic convenience rather than as an attempt to quantitatively model a specific process. We note that in short pulse laser experiments, either a time or frequency domain perspective may be used. In time domain, a standard approach to characterizing the temporal response is time-correlated photon counting, histogramming the photon arrival times and then fitting the characteristic time constants, as is done in fluorescence lifetime imaging [20–25]. In frequency domain, if the excitation beam is modulated, LIA may be used to record an optical response which is phase shifted relative to the input [20,23,26–30]. The LIA phase shift φ is related to the characteristic time constant τ of the photophysical process and the modulation frequency f by:

$$\varphi = -\arctan(2\pi f \tau) \tag{1}$$

If only the lifetime is of interest, it suffices to record the phase shift at each pixel. When both the LIA amplitude and phase are recorded, there are two equivalent methods of representing the signal: in-phase and quadrature (X and Y), or amplitude and phase (R and φ). These are illustrated in Fig. 1. For instantaneous ($\tau = 0$) processes, we see from Eq. (1) that φ is identically zero. In an X-Y representation, these signals appear only along the X axis, with positive signals representing gain and negative signals representing loss. In an R-φ representation, these signals appear at 0° and 180°, again representing gain and loss, respectively. If the process is time-delayed and φ is non-zero, the signal will appear in one of the blue shaded regions in Fig. 1. As an example, a time delayed gain signal is illustrated by the green point in Fig. 1. There is, however, a limit to our experimental ability to distinguish instantaneous from time-delayed processes having short time constants. If we assume there is small amplitude time-independent white noise in the quadrature component, the Y-axis in Fig. 1(a), then our ability to resolve phase representation signals near 0° and 180° is reduced - even when their amplitude is large - as shown by the orange regions in Fig. 1(b): within these regions, we cannot distinguish instantaneous from very short lifetime processes.

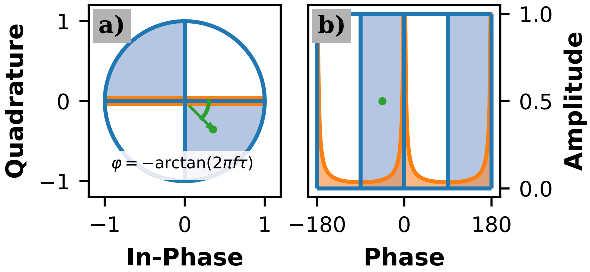

Fig. 1. (a) Quadrature/In-phase $X - Y$ and (b) Amplitude-Phase $R - \varphi$ representations of the raw data collected by a lock-in amplifier (LIA). Different photophysical processes will have differing time responses, ranging from instantaneous (e.g. harmonic generation, Raman scattering) to longer lifetimes (e.g. fluorescence, thermal lensing). The LIA phase shift φ is related to the characteristic time constant τ of the photophysical process and the experimental modulation frequency f through $\varphi = -\arctan(2\pi f\tau)$. The regions shaded blue indicate non-instantaneous ($\tau \neq 0$) processes of finite lifetime. The regions shaded orange illustrate the effects of small amplitude time-independent white noise in the Quadrature / Y channel: LIA signals within the orange regions cannot be experimentally discerned from instantaneous processes. For details, see the text.

A central theme of this paper is that, if more than one photophysical process participates within a single pixel, the analysis becomes more complicated but, as we show here, remains tractable. During any measurement, the different photophysical processes are mixed and detected simultaneously. Precluding nonlinear interactions between these, the resultant LIA phase and quadrature (i.e. X and Y) signals are given by the linear addition of the responses from the individual processes. Interestingly, this can lead to seemingly non-intuitive results when represented in the R-φ domain. To illustrate this and to develop intuition for multi-component responses, we numerically modelled the addition of different nonlinear processes for a spectral focusing SRS implementation wherein the time delay between two pulses is varied. We emphasize that this is an illustrative model with the input parameters chosen to be reflective of experimental observations. The simulations provide valuable intuition on the sometimes complex interactions of various photophysical channels in the signal generation processes. In Table 1, we list different photophysical processes - and their parametrization within our model - which potentially contribute to an experimental SRS image: Raman scattering, cross-phase modulation (XPM) and thermal lensing (TL). In spectral focusing SRS, the amplitude of the Raman signal is a function of the instantaneous frequency difference between two chirped beams and thus changes as a function of time delay. The XPM signal simply tracks the cross correlation of the two input pulses. The TL signal is more complex, as it conceivably obtains over multiple laser pulses [31–35]. It does not typically vary appreciably within the sub-ten picosecond regime but can have an effectively fixed, non-zero phase shifted signal in said regime. For illustrative purposes, the Raman resonant signal is modelled as a single peak having a central frequency of 575 cm^{-1} and linewidth of 11.7 cm^{-1}. For ease of comparison with XPM and TL, we equivalently describe the Raman resonant signal as a pump-probe signal with a 'time zero' at −0.63 ps and width of 0.29 ps. This is due to spectral focusing's property of mapping the frequency-domain Raman information as a time-domain pump-probe signal. In contrast, the XPM signal was chosen here, again for illustrative purposes, to have 'time zero' at 0 ps and width of 1.26 ps. The parameters modelling the Raman Response and XPM correspond to a setup with a spectral resolution of 11.7 cm^{-1} probing an infinitely narrow Raman signal. For the TL response, it is assumed to be long lived such that it is essentially flat and thus has no 'time zero'. We assume in the model that the Raman response leads to a loss and the XPM leads to a gain, corresponding to phases of 180° and 0° respectively. The TL response is illustrated here with a time delay leading to a phase of 120° , corresponding to an apparent lifetime of 276 ns for 1 MHz modulation frequency. Note that all signals are normalized to unit strength at the maximum intensity.

Table 1. Values for the parameters used to model the curves presented in Fig. 2[a]

	Gaussian		Flat Amplitude
	SRL	XPM	TL
Time Zero (ps)	−0.63	0	N/A
FWHM (ps)	0.29	1.26	N/A
Phase (°)	0	180	120

[a] The values are chosen for illustrative convenience, as discussed in the text. Stimulated Raman Loss (SRL) and Cross Phase Modulation (XPM) are represented by Gaussian responses of differing offsets (Time Zero) and widths (FWHM), whereas Thermal Lensing (TL) is represented by a flat response. For instantaneous signals, gains correspond to phase shifts of 0, whereas losses are 180 degrees. All amplitudes are normalized.

Using the parameters described above we show, in Fig. 2, three-dimensional plots of illustrative LIA signals: the X-axis represents the LIA in-phase signal; the Y-axis represents the LIA quadrature signal; the Z-axis represents the Pump-Probe time delay. The XYZ coordinate system is defined in panel (a). The solid orange line represents the total signal for various combinations of the photophysical processes. The dashed orange lines represent the projections onto the X-Y, X-Z, and Y-Z planes. We plot a unit circle in the X-Y plane to help guide the eye to the maximum signal for the different photophysical responses under consideration. The LIA amplitude R is defined in panel (b) as the unsigned magnitude ($|R|$), measured from the origin, of the projection of the (solid orange) signal onto the X-Y plane. The LIA phase φ is defined in panel (c) as the CCW angle in the X-Y plane, measured from the +X axis, of the (solid orange) signal projected onto the X-Y plane. The time delay can be mapped onto an equivalent Raman shift (instantaneous Pump-Probe frequency difference), with both axes shown in middle and bottom rows. In Fig. 2(a), we show a pure XPM response: the signal is zero when the pulses are not temporally overlapped and positive with zero phase shift when the pulses are overlapped in time, as shown by the solid orange line. In Fig. 2(b), we show a system with both XPM and Raman resonant contributions: the signal undergoes rapid variations as a function of time delay, as shown by the orange line. Note that the entire signal remains real: the oscillations are only along the X-axis. In Fig. 2(c), we show the case of XPM and TL: there is a fixed offset in the XY plane due to the TL contribution but the signal otherwise appears similar in form to that of pure XPM.

We argue here that a three-dimensional representation of LIA data facilitates understanding complex, multi-component signals. However, LIA signals are commonly shown as standard two-dimensional representations of the LIA output data: plots of the amplitude R or phase φ versus time delay. In the case of pure XPM, the amplitude Fig. 2(d) is simply a Gaussian and the phase Fig. 2(g) has a constant value of zero; this signal is straightforward to interpret in all representations. When both Raman and XPM are present, the amplitude Fig. 2(e) is identical to the absolute value of the response shown in Fig. 2(b) but the phase, shown in 2(h), switches between 0° and 180°. The addition of XPM and TL results in more complex behaviour for both amplitude Fig. 2(f) and phase Fig. 2(i). When the pulses are not overlapped in time, only the TL signal remains. As XPM increases, the total signal becomes pure quadrature (i.e. phase = 90°)

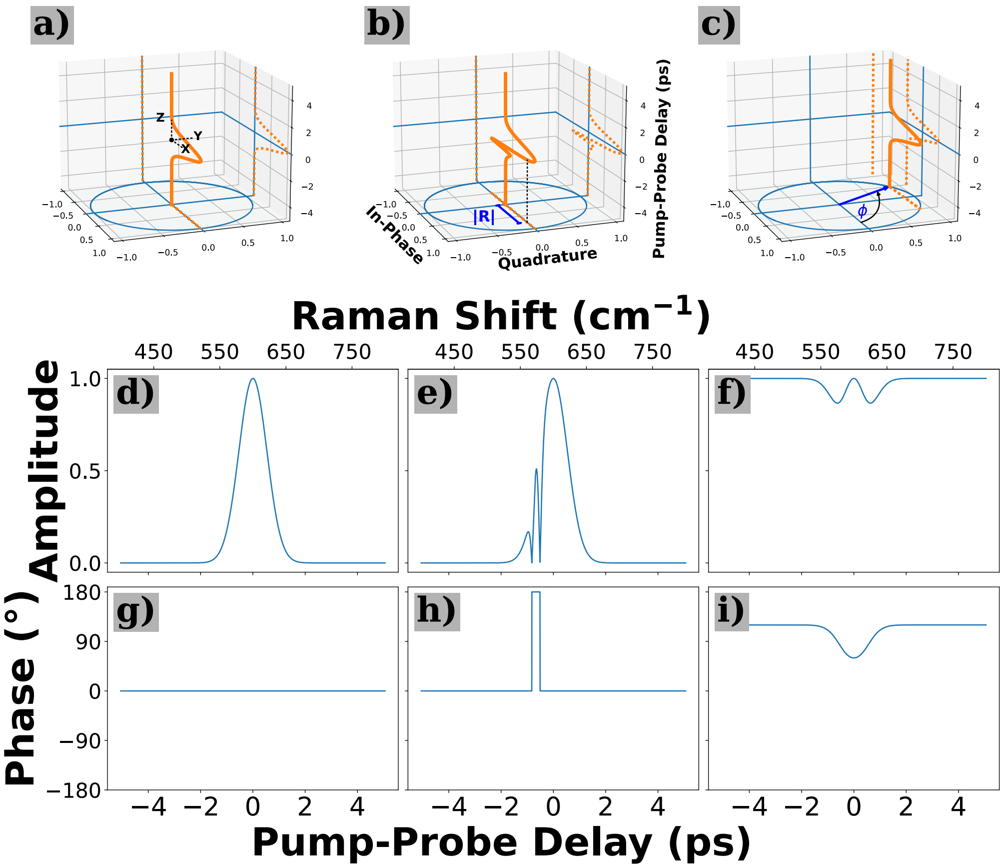

Fig. 2. An illustrative model of Lock-in Amplifier (LIA) output signals versus Pump-Probe time delay for the photophysical processes Cross Phase Modulation (XPM), Stimulated Raman Scattering (Raman) and Thermal Lensing (TL). The top row shows three-dimensional representations of the LIA in-phase (X) and quadrature (Y) signals versus time delay (Z) for: (a) XPM alone, (b) XPM and Raman, (c) XPM and TL. The right-handed XYZ coordinate system is defined in (a). The solid orange line tracks the total signal in each case, its projection onto the X-Y and X-Z planes shown as dashed orange lines. The LIA amplitude $|R|$ is defined in (b) as the unsigned magnitude, measured from the origin, of the projection of the (solid orange) signal onto the X-Y plane. The LIA phase φ is defined in (c) as the CCW angle in the X-Y plane, measured from the +X axis, of the (solid orange) signal projected onto the X-Y plane. The time delay can be mapped onto an equivalent Raman shift (instantaneous Pump-Probe frequency difference): both axes are shown in panels (d)-(i). The second row represents the measured LIA amplitude (R) as a function of time delay for each case: (d) XPM, (e) XPM and Raman, (f) XPM and TL. The third row represents the measured LIA phase (φ) as a function of time delay for each case: (g) XPM, (h) XPM and Raman, (i) XPM and TL. For details, see the text.

and *R* reaches a minimum. At the maximum value of the XPM signal, the total phase is 60° and the magnitude reaches a local maximum. As the XPM signal vanishes with time delay, the total signal returns to the pure TL response. Note that *R* again reaches a minimum during this process.

The addition of XPM and TL, Fig. 2(c), highlights two important general features in the interpretation of LIA signals. First, if a measured LIA signal has a phase between −90° and −180°, or between 0° and 90° (i.e. the white regions in Fig. 1), there must be at least two different photophysical processes contributing to the total signal. Second, in an R-φ representation, the magnitude R is not simply the algebraic addition of two signals when there exists a phase difference between them. Rather, as clarified by this discussion of Fig. 2, R is given by the vector addition of the two processes. This does not, however, preclude determining the magnitudes of the contributing photophysical processes, as we experimentally demonstrate below.

3. Experimental

3.1. Setup

Our custom SRS microscope, depicted in Fig. 3, is based on a FV3000 Confocal Microscope (Evident Scientific, formerly Olympus Lifesciences). Briefly, both beams of a dual output fs oscillator / sync-pumped OPO (Insight X3, Spectra-Physics), with one fixed output at 1045 nm, and a second tunable from 680 nm to 1300 nm, were attenuated using separate half-waveplate polarizer combinations. The fixed arm passed through a Faraday Isolator (IO-3-1064-HP, Thorlabs), an EOM (M360-160, Conoptics) modulated at 1 MHz, and 20 cm of ZnSe. The tunable arm was delayed relative to the fixed arm using a 20 cm travel delay stage (ILS200CC, Newport) before being double-passed through five 10 cm N-SF11 rods (SF11L1100-AR800, Newlight Photonics). The divergence and spot size of the outputs were controlled using separate 1:1 telescopes before being combined at a 1064 nm notch filter (NF1064-44, Thorlabs), angle tuned for use as a dichroic mirror. The combined beams were then introduced to the FV3000 microscope.

The sample introduction objective was a 40x air extended apochromatic objective (UPLXAPO-40X, Evident Scientific). The transmitted beam was collected using a water collection objective (XLPLN25XWMP2, Evident Scientific), filtered using two fluorescence filters (FF01-850/310-25, Semrock) and detected using a Hamamatsu photodiode (S3590-08, Hamamatsu) built into a custom photodetection circuit. The photocurrent was passed through a 50 Ω resistor generating a voltage which was filtered using a 1 MHz, 200 kHz electronic bandpass filter (KR Filters 3128). The filtered signal was subsequently amplified (60 dBV) using a voltage amplifier (Femto HVA-10M-60-B) and then filtered using a 1 MHz, 30 kHz electronic bandpass filter (KR Filters 3149) before being introduced to a lock-in amplifier (UHFLI, Zurich Instruments). All signals were demodulated using the LIA and passed to a built-in external DAQ interface box (FV3000 IO Interface Box, Evident Scientific). The pixel dwell time for all images reported here was 20 μs with a lock-in time constant of 2 μs and a filter order of eight.

3.2. Sample

A lithium ore sample provided by SGS Canada was sieved using a #140 mesh sieve such that all remaining fragments were less than 106 μm in diameter. Before imaging, the powder was dispersed in distilled water, allowed to settle, and then the liquid decanted. This was repeated three times in order to largely remove the sub-micron particulate matter in the sample. After the last rinse, the sample was dispersed a final time in water and deposited onto a 35 mm glass-bottomed Petri dish for imaging.

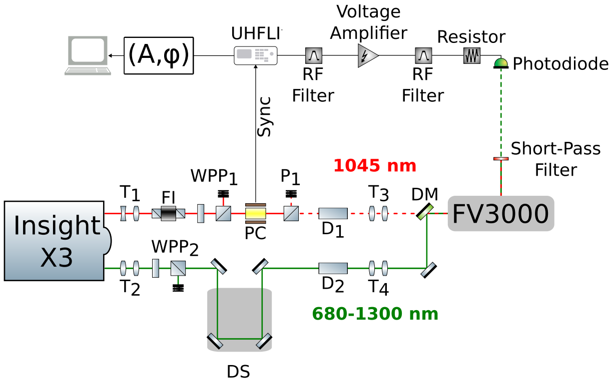

Fig. 3. Schematic diagram of the custom Spectral Focusing SRS microscope. The outputs of an Insight X3 dual output fs oscillator were each expanded to a 3 mm spot size using separate 1:3 telescopes (T_1 and T_2) and controllably attenuated with a waveplate-polarizer combination (WPP_1 and WPP_2). The fixed arm passes through a Faraday Isolator (FI), a Pockels Cell (PC) modulated at 1 MHz, dispersive material (D_1), before going through a 1:1 telescope (T_3). The tuneable arm is delayed relative to the fixed arm using a 20 cm travel delay stage (DS) before passing through dispersive material (D_2) and a 1:1 telescope (T_4). The two beams are recombined using a dichroic mirror before being introduced into a custom FV3000 Confocal Microscope. The transmitted beam is short-pass filtered, with the tuneable arm beam detected by a photodiode whereupon a resistor converts the photocurrent to a voltage, followed by a 1 MHz bandpass filter, a voltage amplifier, and a final 1 MHz bandpass filter before being introduced into a UHFLI Lock-In Amplifier. The Lock-In Amplifier measures both the amplitude and phase of the 1 MHz modulation transferred to the tunable arm beam.

3.3. Signal and phase optimization

In SRS microscopy, the LIA phase can be affected by the position of the microscope condenser lens. The condenser position and the zero-phase setting of the LIA must be optimized before performing measurements. This was achieved using a calibration standard comprised of a dual component mixture of Potassium Dihydrogen Phosphate powder, KH_2PO_4 (KDP), and 4-Acetamidophenol powder, embedded in cyanoacrylate glue. The condenser position was finely adjusted so as to maximize the signal amplitude for the 4-Acetamidophenol Raman shift at 857.9 cm^{-1}, a large and well characterized SRS resonance. At this condenser position, the LIA phase offset was adjusted to zero, consistent with the assumption that SRS is an instantaneous process on the timescale of the laser pulses.

4. Results

4.1. Spectral analysis

Standard mineral analysis techniques determined that the lithium ore sample studied here contained quartz SiO_2, feldspars $MAl(Al,Si)_3O_8$ where M = Na, K or Ca, and the economic lithium ore spodumene $Li[AlSi_2O_6]$. These have well-known characteristic Raman peaks at 463 cm^{-1} (quartz), 508 cm^{-1} (feldspar) and 708 cm^{-1} (spodumene) [36]. An SRS image at each Raman shift of interest was recorded and overlaid to create an RGB merge, shown in Fig. 4. Here, the 463 cm^{-1} image is red, the 508 cm^{-1} image is green and the 708 cm^{-1} image is blue. As can be seen in Fig. 4, regions 1-4 are relatively monochromatic and readily assigned to quartz (region 1, red), feldspar (region 2, green) and spodumene (region 3 and 4, blue). In Fig. 5, we show the

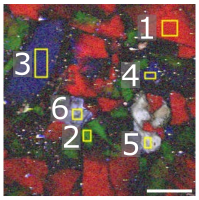

Fig. 4. False-Colour composite image of a lithium ore sample with specific Regions of Interest (ROI) selected and labelled 1-6. Three images were taken at three different Raman shifts and then RGB merged. The white scale bar corresponds to 75 µm. The gamma is set to a value of 0.25, and the minimum amplitude was adjusted to improve the visibility of low signal regions. The false colours correspond to Raman shifts of 463 cm^{-1} (red, quartz), 508 cm^{-1} (green, feldspar), and 708 cm^{-1} (blue, spodumene) [36]. The grey/white ROIs 5 and 6 indicate that more that one photophysical process or species must contribute to the image intensity.

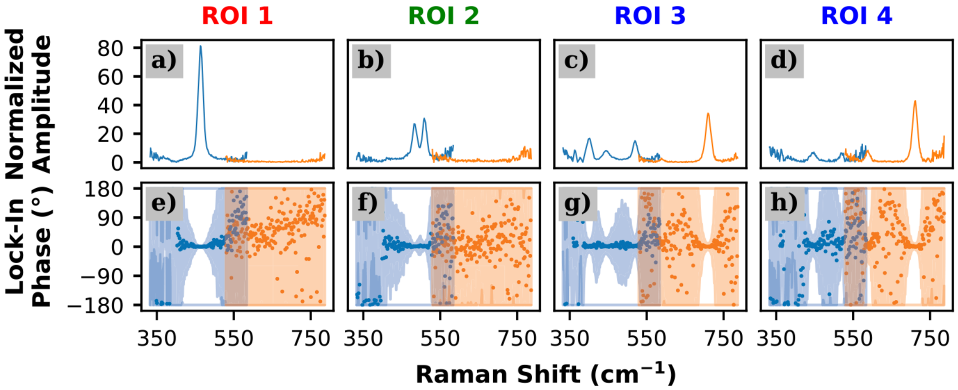

Fig. 5. Lock-in amplifier amplitude and phase spectra for ROIs 1-4 of Fig. 4. In these spectral focusing pump-probe scans, the time delay is represented here as a Raman shift. The upper row shows the normalized lock-in amplitude spectra over the 300-800 cm^{-1} range, the lower row shows the corresponding lock-in phase spectra. The shaded regions in the phase spectra indicate the standard deviation of the phase. The blue spectra were collected using a pump wavelength of 998 nm, centred at a Raman shift of 450 cm^{-1}. The orange spectra were collected using a pump wavelength of 979 nm, centred at a Raman shift of 650 cm^{-1}. The anti-correlation between signal amplitude and standard deviation of the phase is expected, as the lock-in phase becomes indeterminate when the signal amplitude approaches zero.

associated Raman spectra in Fig. 4 for regions 1-4. The LIA amplitude and phase outputs are shown in the top and bottom rows, respectively. The amplitude spectra confirm the assignment.

Although regions 3 and 4 contain the same material, there are notable differences in the Raman spectra within Region 3, showing several additional peaks at low wavenumbers. This differential behaviour is due to crystallite orientation effects; the relative orientations of the micro-crystallites relative to the input laser polarizations, combined with the polarization-dependent Raman selection rules, leads to crystallite-dependent Raman spectral amplitudes. For regions 1-4, the LIA phase provides little additional benefit for species classification. The processes occurring within these regions appear instantaneous, leading to LIA phases of either 0° or ±180°. We note the anticorrelation between the standard deviation of the phase with the absolute signal amplitude at a given Raman shift. This is simply due to the fact that, when the signal amplitude is high, the phase uncertainty is much smaller.

While regions 1-4 in Fig. 4 are monochromatic, suggesting a single dominant optical response, Regions 5 and 6 are grey and white, demonstrating strong optical responses at multiple Raman shifts. Under such circumstances, measuring only the amplitude at a single Raman shift will not suffice to classify mineral species in these regions. Significantly, the grey/white colour indicates a broadband response, likely meaning that several photophysical processes contribute to the image intensity in that region. We note that the dangers of imaging at a single SRS Raman shift for classification and segmentation purposes were previously discussed [19]: it was recommended to record broader Raman spectra at each pixel (hyperspectral imaging), in that case using spectral focusing SRS.

The spectra recorded in regions 5 and 6, shown in Fig. 6, show peaks substantially broader than those of regions 1-4. As detailed below, we can extract characteristic information about the sample based upon consideration of the differing photophysical processes involved. For example, in region 5, the amplitude response is relatively flat with respect to time delay, as shown in Figs. 6(a) and 6(b), suggesting the photophysical process involved does not depend strongly on the pump-probe time delay. This response is consistent with single-photon excited thermal lensing (TL) or transient absorption (TA) signals, both of which have lifetimes typically exceeding the cavity roundtrip delay between laser pulses (12.50 ns for the 80 MHz laser used here) [7,37]. This interpretation is further supported by the phase response measured in Region 5. As seen in Figs. 6(e) and 6(f), at both excitation wavelengths the phase is nearly constant at −71° ± 4° over the entire range. This corresponds to an equivalent lifetime of 500 ns ± 100 ns, consistent with the suggestion that the predominant signal amplitude in this region is thermal in nature.

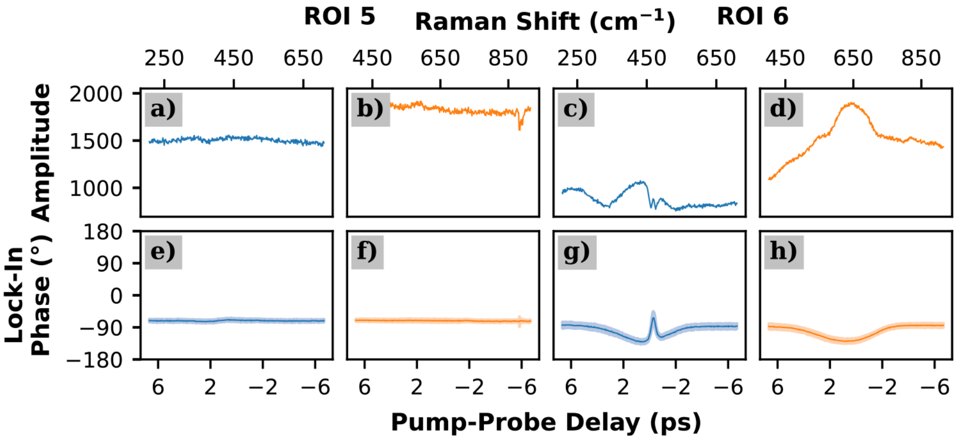

Fig. 6. Lock-in amplifier amplitude and phase spectra for ROIs 5-6 of Fig. 4. The scans are represented as both pump-probe time delay (bottom axis) and Raman shift (top axis). Differing from the spectra of Fig. 5, ROIs 5-6 are not dominated by Raman processes: they comprise more complex photophysical processes. Here, the top row is the un-normalized signal amplitude. The bottom row is the corresponding lock-in phase, with its standard deviation shown as shaded regions. The blue spectra (panels a), c), e), and g)) were recorded using a pump central wavelength of 998 nm (a central Raman shift of 450 cm^{-1}). The orange spectra (panels b), d), f), and h)) were recorded using a pump central wavelength of 979 nm (a central Raman shift of 650 cm^{-1}). As the signal amplitude remains large over the entire spectral range, the corresponding phase is well defined. For details, see the text.

The structure of the amplitude spectrum of Region 6, shown in Figs. 6(c) and 6(d), is more complex than in any other measured region. Two features are notable: (i) there is a peak at roughly 463 cm^{-1}, consistent with the Raman response of quartz; (ii) for each pump excitation central wavelength, the signal is asymmetric with respect to time zero (the maximum in the pump-probe cross-correlation). The blue curve, corresponding to a pump wavelength of 998 nm, is substantially more structured. This behaviour is readily understood using the phase data shown in Fig. 6(g). The phase offset when the pulses are not temporally overlapped indicates that a photophysical process with a slow time response must contribute to the overall system response. There is additionally a spectrally broad signal which follows the temporal cross-correlation of the two pulses; this suggests an additional contribution from a non-resonant, nearly instantaneous photophysical process. A spectrally sharp feature is seen in the phase spectrum, at roughly 463 cm^{-1}. There is a similar feature in the amplitude spectrum, assigned to the Raman response of quartz. With reference to the discussion of Figs. 2(e) and (h) above, we note that there are four time delays where the phase crosses 90° in the phase response recorded with the 998 nm central wavelength: these correspond to four minima seen in the amplitude spectrum of Fig. 6(c). The phase response for a pump central wavelength of 979 nm is shown in Fig. 6(h) and is similar, however now without any Raman-like features.

In order to extract all available information from the blue curve of Fig. 6(g), we applied a multi-component fit to the phase data, shown in Fig. 7. Specifically, we fit the phase signal to $1/\tan\varphi{=}(X/Y)$ which is extracted directly from the LIA via the ratio of the in-phase (X) and the quadrature (Y) components. Based on the discussion of Fig. 2, above, on different photophysical contributions to the total signal, our fitting procedure assumed a linear combination of three components: two Gaussians and a constant offset baseline. The fit to the baseline component corresponds to a phase shift of $-86.245° \pm 0.002°$, consistent with an apparent lifetime of 2.43 ± 0.08 µs. The fit to the first (spectrally sharp) Gaussian is centered at 467.69 ± 0.07 cm^{-1}, with a narrow FWHM of 17.1 ± 0.2 cm^{-1}. This roughly matches the well-known Raman resonance in quartz, supporting the assignment based on the sharp features in the amplitude spectrum. The fit to the second (broad) Gaussian is centred at 437.7 ± 0.2 cm^{-1} and has a very broad FWHM of 145.1 ± 0.8 cm^{-1}. This does not correspond to any known Raman features and is therefore likely due to non-Raman processes. To investigate further, we compared these signals with a simultaneously measured Gaussian temporal cross-correlation of the pump and Stokes pulses, using SFG within the quartz present in the sample. Comparing the Gaussian fit to the phase data of Fig. 6 with the Gaussian SFG cross-correlation signal, we find that the former is shifted in time by 291 ± 8 fs and its FWHM increases by 180 ± 20 fs. This suggests the broad Gaussian signal in the sample is due to an instantaneous or nearly instantaneous response. Indeed, this signal is exactly out-of-phase with the SRS signal, consistent with a near instantaneous response. This apparently instantaneous lifetime is well within the pump-Stokes Cross-Correlation, suggesting that a Gaussian fit is a reasonable approximation. We note, however, that the observed out-of-phase shift rules out Non-Degenerate Two-Photon Absorption (ND-2PA): since absorption is a loss, it would be in-phase with the SRS signal in our Stimulated Raman Loss configuration. Taken together, the broad, nearly instantaneous response is consistent with either Cross-Phase Modulation (XPM) or Transient Absorption (TA). Unfortunately, we are unable to further discern these within our present implementation.

4.2. Full spectrum segmentation

SRS microscopy permits identification and quantification of the chemical species of interest within the sample. For the mineral samples studied here, this requires assigning a chemical/mineral identity to each pixel. Within these specific samples, the material is composed of sets of distinct grains: we therefore assume, for simplicity, that each pixel is comprised of a single pure material. In order to identity the mineral/chemical species at each pixel, we calculated the degree of similarity between the recorded pixel-specific SRS spectrum and a set of standard reference spectra. We previously identified the different species of interest using the SRS spectra recorded in ROIs 1-3 where the Raman resonant response strongly dominates: these comprise our standard

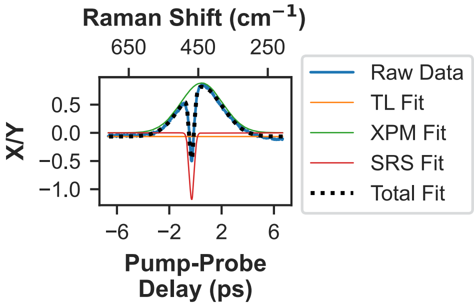

Fig. 7. The phase spectrum shown in Fig. 6(g), corresponding to ROI6, shows evidence of several photophysical processes contributing to the total signal. A multi-component least squares fit was applied to these data, plotted here as a function of pump-probe time delay for the ratio X/Y of the LIA in-phase (X) and the quadrature (Y) signals. This ratio is directly related to the LIA phase φ by $1/\tan\varphi = (X/Y)$. The blue curve shows the raw experimental data. The orange curve corresponds to the fitted baseline offset, assigned as Thermal Lensing (TL). The green curve corresponds to a Gaussian fit centred at 437.7 ± 0.2 cm^{-1} with a FWHM of 145.1 ± 0.8 cm^{-1}, assigned as Cross-Phase Modulation (XPM). The red curve corresponds to a Gaussian fit centered at 467.69 ± 0.07 cm^{-1} with a FWHM of 17.1 ± 0.2 cm^{-1}, assigned to the resonant SRS signal from quartz. The total fit (dashed black curve) corresponds to the sum of the orange, green, and red curves and shows excellent agreement with the experimental data (blue).

reference spectra. At each pixel, we solved the equation:

$$I_i = I_{ij}^{(r)} M_j \tag{2}$$

where I_i is the normalized spectrum at pixel i, $I_{ij}^{(r)}$ is the normalized reference spectrum for material j, and M_j is a vector giving the composition in terms of the materials j. Calculating the Moore-Penrose pseudoinverse provides the least-squares solution for M_j where each element corresponds to the spectral overlap. In our dataset, M_j is a 3-element vector which we plot as an RGB image, with red corresponding to species 1 (quartz), green to species 2 (feldspar) and blue to species 3 (spodumene). A fitting procedure performed using only the 1D amplitude R (real-valued) data is shown in Fig. 8(a). Importantly, as both LIA amplitude R and phase φ data were recorded at each pixel, we developed a more advanced fitting procedure which makes use of 2D (R, φ) (complex-valued) data, the results being shown in Fig. 8(c). The comparison of these 1D and 2D approaches to segmentation is discussed below.

In our approach to segmentation, the resultant vector M_j was fitted, using Variational Bayesian estimation, to a Gaussian Mixture Model comprised of seven components. The seven components are: spodumene, feldspars, quartz, two types (i.e. differing phase response) of thermal lensing, background pixels, outliers. The fit assigns to each pixel the probabilities for each component: the pixel is fully assigned to the probability component of greatest magnitude. This procedure yields spectral cross-correlation masks which permit assignment of each pixel to the different materials comprising the sample. These are presented in Fig. 8(b) for 1D fitting and in Fig. 8(d) for 2D fitting. Due to the properties of this sample, our ability to perform a proper cross-validation of the segmentation against alternative methods is limited. This required us to develop an internal validation procedure, discussed below.

There are three regions of interest labelled from I to III in Fig. 8(b) where the 1D and 2D fitting procedures disagree. Analysis of these regions provides details allowing us to directly compare and contrast the 1D and 2D approaches to segmentation. We begin with Region I. The amplitude spectrum, Fig. 9(a), shows two spectral regions: a sharp peak at 708 cm^{-1} and a series

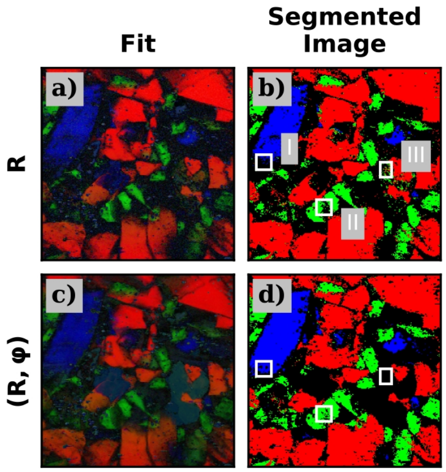

Fig. 8. Segmentation of mineral species using Raman spectral data. Using least squares fitting at each pixel, the spectral overlap with predefined masks (standard reference Raman spectra) was determined. a) 1D (real-valued) fitting. Using only amplitude R data, the spectral overlap of each component with its mask was calculated via Moore-Penrose pseudoinverse, yielding an RGB map (red is quartz, green is feldspar, blue is spodumene). b) Using a Gaussian Mixture Model with seven components, fitted to the image in a), we show the aggregated RGB histogram resulting in this segmented image. c) 2D (complex-valued) fitting. Using 2D (amplitude, phase) = (R, φ) data, the spectral overlap of each component with its mask was calculated (red is quartz, green is feldspar, blue is spodumene). d) Fitted to Gaussian Mixture Model as in b), now using the 2D (R, φ) data shown in c). The aggregated RGB histogram produced the resulting segmented image. It can been seen in that finer details within the segmented image d) can be resolved using the 2D fit. The differences between 1D and 2D segmentation are discussed in the text.

of peaks between 350 and 550 cm^{-1}. As seen in the phase spectrum Fig. 9(d), these peaks are all associated with a phase shift of zero, indicating Raman resonant processes. This permits, uniquely, the assignment of Region I to spodumene. Region II shows sharp features at 479 and 508 cm^{-1} in Fig. 9(b) and, at each resonance, a phase shift of zero in Fig. 9(e). This permits, uniquely, the assignment of Region II to feldspars. Region III shows no sharp features in Fig. 9(c) and, critically, has a near constant phase shift of $-71°$ as seen in Fig. 9(f). This confirms that image intensity in Region III cannot be attributed to Raman resonant processes and is more likely due to thermal lensing. We assign it to an unknown material which has a thermal response. For each region examined here, we find that the 2D fitting procedure provides more accurate segmentation than the 1D approach and improves the extraction of small (close to the noise floor) signals.

Given the success of the 2D fitting procedure, we define it to be the reference segmentation for the sample. We quantify the differences between the 1D amplitude versus 2D amplitude-phase masks using three parameters: the Intersection Over Union (IOU), the Precision, and the Recall. The IOU is the total deviation from a reference mask (here, the masks given by Fig. 8(d)). The Precision is the ratio of the true positives (TP) to the sum of the true (TP) and false (FP) positives. The Recall is ratio of the true positives (TP) to the sum of the true positives (TP) and false negatives (FN). Mathematically, the IOU, Precision and Recall are given by Eqs. (3a)–(3c), respectively. We note that (TP) is the number of pixels which are nonzero in both the reference image and the image under comparison; (FP) is the number of pixels which are nonzero in the image under comparison but are zero in the reference image; (FN) is the number of pixels which

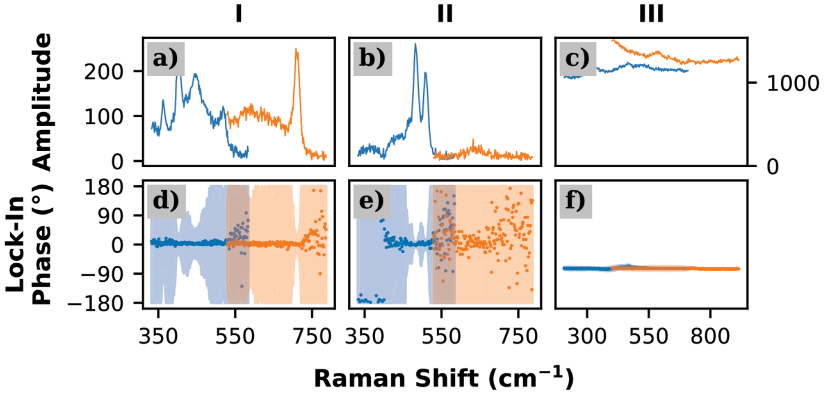

Fig. 9. Comparison of image segmentation results obtained from use of the 1D and 2D spectral cross-correlation masks presented in Figs. 8(b) and (d), respectively. The 2D mask, making use of 2D amplitude-phase correlations, permits more accurate segmentation: Raman resonant processes must have a phase shift of zero. Amplitude (top row) and Phase (bottom row) spectra are presented, as columns, for the Regions I-III as labelled in Fig. 8(b). The amplitude spectra share a common y-axis (left) for Regions I and II, whereas Region III, due to its differing amplitude, has a unique y-axis (right). The shaded regions in the phase spectra represent a single standard deviation. As detailed in the text, the 2D mask approach, Fig. 8(d), uniquely assigns Region I to spodumene and Region II to feldspars. The 2D mask analysis further reveals that pixels within Region III of Fig. 8(b) were incorrectly assigned by the 1D mask to quartz and feldspars: they cannot be due to their non-zero phase shift, as shown in f). For details, see the text.

are nonzero in the reference image but are zero in the image under comparison.

$$\text{IOU} = \frac{TP}{TP + FP + FN} \tag{3a}$$

$$\text{Precision} = \frac{TP}{TP + FP} \tag{3b}$$

$$\text{Recall} = \frac{TP}{TP + FN} \tag{3c}$$

In Table 2, we show the results of 1D segmentation into the three mineral species quartz, feldspar and spodumene. For quartz, the IOU of 0.866 suggests a strong match. This is confirmed by the Precision and Recall, where the Precision of 0.888 suggests that there are some false positives while the Recall of 0.971 suggests effectively no false negatives. For feldspar, the IOU is 0.693, the Precision is 0.856, and the Recall is 0.785. In this case, the classification/segmentation found most of the true positives, but the greater green false assignments seen in the image shows that noise is being incorrectly segmented as feldspar. Furthermore, the Recall suggests that there are pixels missed by the segmentation. Finally, for spodumene the IOU is 0.711, similar to that of feldspar. The Precision of 0.987 shows that there are almost no false positives but the Recall of 0.718 indicates that a significant number of pixels corresponding to spodumene are missed.

4.3. Rapid imaging: single frame analysis from 2D amplitude-phase correlations

While using full Raman spectral analysis is preferred for pixel classification/segmentation, it requires hyperspectral imaging, a substantially longer data collection effort compared to an image recorded at a single Raman shift. However, previous studies using ps pulse SRS microscopy showed that the LIA phase can be used as as an additional source of contrast [11,12]. Here we

Table 2. Parameters quantifying the 1D Amplitude-Only segmentation[a]

Material	Intersection over Union	Precision	Recall
Quartz	0.866	0.888	0.971
Feldspar	0.693	0.856	0.785
Spodumene	0.711	0.987	0.718

[a] The quantification of the segmentation is performed relative to a reference segmentation of the 2D Correlated Amplitude-Phase segmentation.

extend this approach to 2D amplitude-phase correlations. To demonstrate this, we consider a single frame (i.e. single Raman shift) extracted from the full hyperspectral dataset. In Fig. 10(a), we show the amplitude signal corresponding to the blue channel in Fig. 4. This was recorded at a Raman shift of 708 cm^{-1}, assigned to spodumene. Using 1D amplitude data alone, it is impossible to determine the relative contributions of SRS, some form of time-delayed process or a mixture of nonlinear processes. However, at each pixel, we can simultaneously record the LIA In-Phase (X) and Quadrature (Y) signals. This permits construction of the 2D correlation plot shown in Fig. 10(b) in the X-Y representation. In Fig. 10(c) we show this 2D correlation plot in the R-φ representation. It is immediately evident that there are multiple photophysical processes operating, of different amplitude-phase correlations, which contribute to the overall image intensity. Interestingly, the brightest regions in Fig. 10(a) (i.e. the highest amplitude) do not occur near 0° phase and therefore do not correspond to an SRS process.

The 2D plots Figs. 10 b) and c) reveal four distinct correlation regions which can be used to discern the underlying photophysical processes. For clarity, these different correlation regions are labelled in Fig. 10(b). Region I, in black, corresponds to pixels with low signal and a distribution which favours neither the In-Phase nor Quadrature Signals. Given the weak signals, it was not possible to determine which, if any, of the nonlinear signals contribute to these pixels and they are treated as background. Region II, in blue, is almost purely In-Phase signal (corresponding to an average phase of -0.72) and is of considerable magnitude, suggesting that it corresponds to purely Raman signals. Region III, in yellow, is large and comprised of a mixture of In-Phase and Quadrature signals, the average phase being -68.69 (close to the average phase for region 5 in Fig. 6(c). This indicates that the signal from pixels corresponding the Region III is largely due to thermal lensing. Finally, Region IV, in magenta, has an average phase of $-108.94°$ close to the average phase for ROI 6 in Fig. 6(d). This indicates that several different photophysical processes contribute to image formation in this correlation region.

Applying the Gaussian Mixture Model fit to this image yields the segmentation presented in Fig. 10(d), where the colours correspond to the regions previously defined in Fig. 10(b). The pixel-level 2D amplitude-phase correlations provide two advantages. First, they allow for the enhanced classification and segmentation of materials based on their differing photophysical processes, as shown in Fig. 10(d). Second, there is an inherent noise reduction associated with this approach to segmentation.

This can be quantified by comparing against a Multi-Otsu Segmentation to create four regions (shown in Supplement 1 Fig. S1 as a comparison between Fig. 10(d) and the mask created by this segmentation). In comparison to the reference segmentation found using the 2D fitting procedure, the IOU, Precision, and Recall for the Multi-Otsu segmentation are 0.44, 0.52, and 0.75, respectively, whereas for the Gaussian Mixture Model they are 0.71, 0.82, and 0.83, respectively. The quality of the latter segmentation is much better, evidenced by the IOU and the Precision, with the dominant effect being the reduction in false positives, achieved by separating

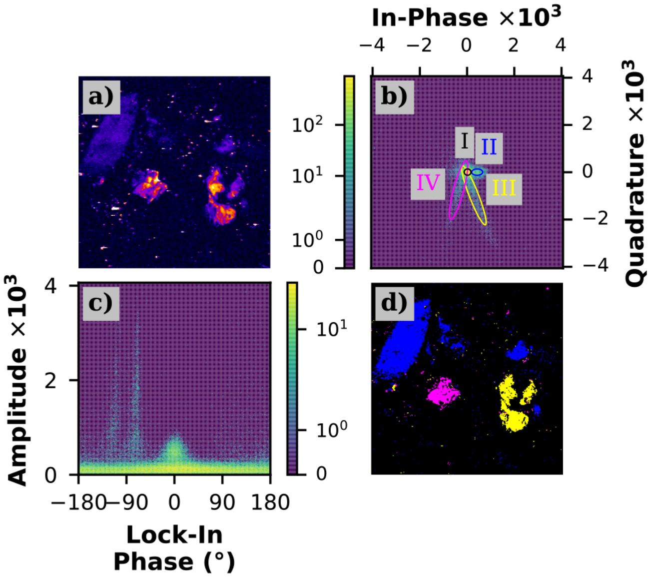

Fig. 10. Lock-in amplifier 2D Amplitude-Phase correlations demonstrate enhanced image segmentation. a) Standard amplitude image for the frame corresponding to a Raman shift of 708 cm^{-1} in Fig. 4. b) 2D histogram of the in-phase (X) versus quadrature (Y) lock-in signals for each pixel in a). Overlaid on the histogram are four regions corresponding to different signal types with distinguishable correlation maps. I (black) is attributed to noise, II (blue) is attributed to pure Raman signals, III (yellow) is attributed to thermal lensing and IV (magenta) is attributed to a combination of nonlinear optical processes. c) 2D histogram of the amplitude (R) versus phase (φ) for each pixel in a), clearly showing distinct correlation maps. d) 2D segmentation of the image using a Gaussian Mixture Model with six components, of which three are displayed. Note that the regions presented in b) correspond to four of the six regions used in the model.

out regions exhibiting time-delayed processes. There is a further improvement through a small reduction in the number of false negatives as seen by the increase in the Recall from 0.75 to 0.83.

4.4. Bilateral filtering

We discuss here an alternative approach to noise reduction, Bilateral Filtering, which makes use of both spatial and spectral proximity information in neighbouring pixels. The net result is a filtered image with reduced noise and better preservation of spatial boundaries between differing materials.

An initial attempt might be to perform Bilateral Filtering using 1D amplitude data alone. However, as discussed for single frame data sets, it can be difficult to distinguish Raman from non-Raman signals using only 1D amplitude data: we demonstrated above that 2D amplitude-phase correlations within each pixel leads to improved filtering. Therefore, in order to proceed, we compute x, defined as a filtered image which minimizes the following equation:

$$\underset{x}{\text{minimize}}\ \frac{\lambda}{2}\sum_{i,j} W_{i,j}\left(x_i - x_j\right)^2 + \sum_i (x_i - t_i)^2 \tag{4}$$

where t is the original image, λ is the weight of the smoothing term, and $W_{i,j}$ is a data-dependent affinity matrix [38]. This affinity matrix is constructed as follows:

$$W_{i,j} = \exp\left(-\frac{\|[p_i^x, p_i^y] - [p_j^x, p_j^y]\|^2}{2\sigma_{xy}^2} - \frac{\|[p_i^{\Re}, p_i^{\Im}] - [p_j^{\Re}, p_j^{\Im}]\|^2}{2\sigma_{\Re\Im}^2}\right)$$

where the variables p_k^x, p_k^y, $p_k^{\Re}$, $p_k^{\Im}$ are, respectively, the horizontal spatial coordinate, the vertical spatial coordinate, the in-phase LIA component, and the quadrature LIA component for pixel k. The σ_{xy} and $\sigma_{\Re\Im}$ control the strength of the affinity, based on spatial proximity and LIA signal similarity, respectively.

In Fig. 11, we compare different approaches to segmentation of the raw image presented in Fig. 4. For each approach, the segmented component images for quartz, feldspar and spodumene are shown in three columns. The right hand column shows, for each approach, the resulting merged images in panels d), h), and l). In the top row (reference segmentation) panels a), b) and c), the masks applied to Fig. 4 were based on Gaussian Mixture Modelling of the full hyperspectral data stack, using the detailed procedure presented in section 4.2. We take this top row to be an effective reference segmentation, permitting comparison with other (more rapid) segmentation approaches. The middle row (Single Frame) panels e), f) and g) show the results of rapid single-frame analysis with Gaussian Mixture Modelling (described above) applied to Fig. 4. In the bottom row (Bilateral Filter), Bilateral Filtering was subsequently applied (before segmentation) to the middle row single-frame panels e), f) and g). In both the middle and bottom row panels, the values of IOU, Precision and Recall are inset, quantifying the segmentation results relative to the (reference segmentation) top row panels a), b) and c).

As shown in Fig. 11 e)-h) and section 4.3 above, 2D amplitude-phase correlations permit segmentation of single frame images which are reasonable matches to the reference segmentation images. In particular, the quartz and spodumene components are particularly strong matches, as shown by their IOU values of 0.72 and 0.71 respectively. The quality of the segmentation for the feldspar, however, is notably worse, with an IOU of 0.41. The Precision values of 0.87, 0.70 and 0.82 for quartz, feldspar and spodumene, respectively, suggest that Gaussian Mixture Modeling does a reasonable job at extracting the features present in the image. The Recall values of 0.80, 0.49 and 0.83 for quartz, feldspar and spodumene, respectively, suggest that quartz and spodumene segmentation extracts most features without many false negatives. Feldspar segmentation, however, noticeably suffers at low signal levels.

Upon Bilateral Filtering, Fig. 11(i)-(k), the IOU values for the three materials become 0.79, 0.55, and 0.75, respectively. Concomitantly, the Precision values become 0.87, 0.64 and 0.82 and the Recall values become 0.89, 0.80 and 0.90. These results demonstrate an important advantage of Bilateral Filtering: it reduces the false negatives rate in image segmentation. Interestingly, there appears to be little benefit of Bilateral Filtering for the false positives rate, as indicated by these Precision values.

The trends observed for the Single Frame (middle row) and Bilateral Filter (bottom row) approaches can be rationalized via their 2D Amplitude-Phase correlation histograms, an example being given in Fig. 10 c). All other 2D Amplitude-Phase correlation histograms for these data are presented in Supplement 1 Fig. S2.

We consider the Single Frame approach (middle row) and remark on two points relevant to this analysis. First, the largest observed signals increase in order from feldspar, spodumene to quartz. Second, the 2D Amplitude-Phase correlation histograms for quartz and spodumene are well above the baseline noise, whereas that of feldspar overlaps non-negligibly with baseline noise. In the Single Frame (middle row) images, the Recall values correlate with the maximum signal, suggesting that signal strength is an important factor in determining the image area occupied by a given component. In effect, stronger signals enable better definition of the boundary edges for a given component. The dominant factor determining the Recall values

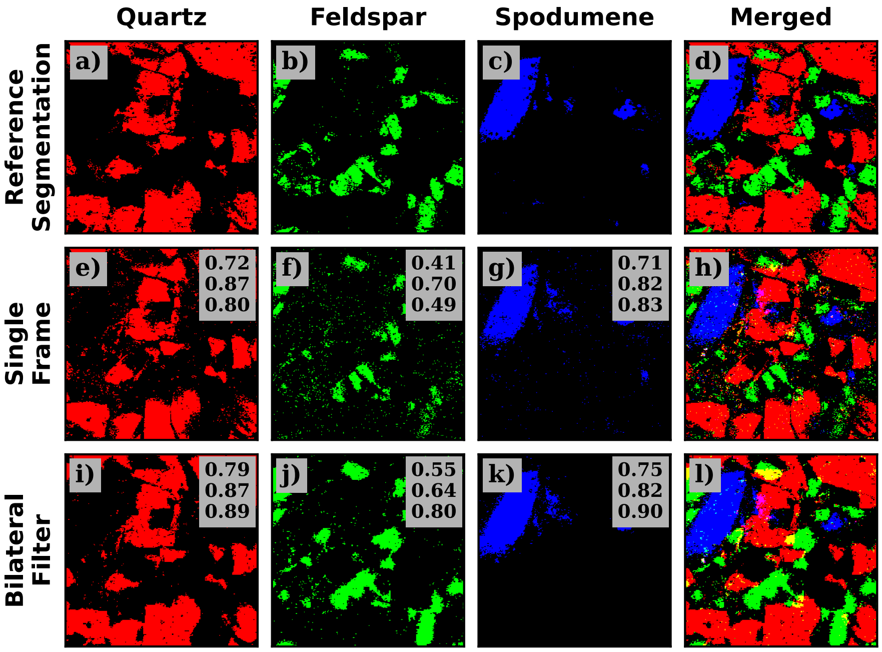

Fig. 11. A comparison of the masks produced using the method presented in Sec. 4.2. The top row, which we take to be an effective reference segmentation, corresponds to the full hyperspectral masks produced for Fig. 8(d). In the second (Single Frame) and third (Bilateral Filter) rows, individual frames were fitted using Gaussian Mixture Modeling to extract the Raman-resonant components. Inset in each second and third row images are three values which correspond to Intersection over Union, Precision, and Recall, relative to the reference segmentation frames shown in the top row.

is likely the distance of the signal distribution from the background/noise floor. For the quartz and spodumene, the distributions are well above the noise floor, allowing a relatively clean segmentation from the background/noise. In contrast, the feldspar distribution overlaps considerably with the background/noise floor, increasing both false positives and false negatives. A factor contributing to this difficulty is that the Gaussian Mixture Modeling approach is a histogram-based segmentation which does not consider any spatial information.

We consider now the Bilateral Filter approach (bottom row), a post-processing method which makes use of spatial information. Importantly, the Recall values demonstrate that Bilateral Filtering improves both edge definition and the recognition of regions with weaker signals. We suggest, therefore, that Bilateral Filtering be included among the post-processing techniques used to enhance image segmentation. There is a signal-to-noise limit, however, to the advantages of Bilateral Filtering, illustrated here in the feldspar segmentation. We note that the Precision values generally do not increase and actually decreases for feldspar. This indicates that the number of false positives relative to the number of true positives has increased, despite the observable decrease in the number of random false positives seen far from other crystallites. The feldspar edges seem to be over-defined relative to the reference segmentation, leading to the observed trend in the Precision values. The observed degradation in the feldspar case is due to the overlap of its 2D Amplitude-Phase correlation histogram with the background/noise, thus reducing the efficacy of Bilateral Filtering.

5. Conclusion

We have argued that it is useful to consider spectral focusing SRS microscopy as a form of Pump-Probe microscopy wherein the signal behaviour with respect to the modulation time scale may contain additional information. Governed by the underlying light-matter interactions, certain photophysical signals must be instantaneous with respect to the modulation (e.g. Raman scattering, cross-phase modulation) whereas others are not (e.g. thermal lensing). Importantly, the lock-in amplifier, commonly used in SRS and Pump-Probe imaging, permits simultaneous collection of both amplitude and phase (i.e. in-phase and quadrature) signals. We demonstrated here that 2D Amplitude-Phase correlations can be used advantageously in order to distinguish nonlinear optical processes - or mixtures of processes - which contribute to image formation, leading to improved image segmentation.

As shown previously for ps-AM-SRS [11,12], the LIA phase channel can be used to enhance contrast even for single frame (i.e. single Raman shift) images. We have leveraged 2D Amplitude-Phase correlations to generally improve segmentation quality in several ways. First, well-known techniques for data reduction (e.g. the linear regression of Sec. 4.2) which make use of this 2D information lead to demonstrably improved segmentation quality by better extracting low signal features while simultaneously reducing spurious false assignments. Second, in Sec. 4.3 we showed that 2D Amplitude-Phase correlations applied to even single frame images retain enhanced segmentation quality at much faster data rates. Finally, in Sec. 4.4, we showed that Bilateral Filtering, which makes additional use of spatial correlations, can be used to further improve the specificity of targeted denoising approaches.

These simple and readily available methods have been shown to be advantageous for several different forms of nonlinear microscopy [29,39,40]. The often neglected LIA phase is an extra channel of complementary information regarding the photophysical processes contributing to the signal at each pixel. We suggest that, for modulation schemes more complex than the standard AM-SRS microscopy discussed here, there will be advantages to recording 2D Amplitude-Phase correlations. For example, in the case of Polarization Modulation-SRS [41], a known issue is that it is challenging to remove all background signals simultaneously and that residual amplitude modulation may contribute to the measured signals. In general, we expect that, for any SRS modulation scheme, 2D Amplitude-Phase correlations will help better discern Raman from non-Raman (i.e. background) processes. Furthermore, we believe that more sophisticated schemes such as SRGAL [42], wherein the two input beams are modulated at different frequencies such that both SRG and SRL can be measured simultaneously, will benefit considerably from this approach: the LIA phase of the non-Raman signals will depend on whether SRG or SRL is detected and, therefore, 2D Amplitude-Phase correlations will enhance segmentation and process identification beyond what is currently achievable. We anticipate that the general methods presented here will lead to an improved understanding of image formation in nonlinear optical microscopy and, therefore, improved image classification and segmentation, the demonstration of which is important for its even broader acceptance.

Funding. Natural Sciences and Engineering Research Council of Canada (13594979, Discovery Grant Program, RGPIN-2022-05325); National Research Council Canada (AI4D-124-1, QSP-052); Canadian Foundation for Innovation; Max-Planck-Centre for Extreme and Quantum Photonics; Canada Research Chairs.

Acknowledgments. We thank the NRC NPO AI for Design grant # AI4D-124-1 and the NRC NPO Quantum Sensors program grant #QSP-052 for financial support. We additionally thank NSERC, the NRC-uOttawa Joint Centre for Extreme Photonics (JCEP) and the Max-Planck-uOttawa Centre for Extreme and Quantum Photonics for support. Alexander N. Harper thanks the OGS for financial support. The authors acknowledge fruitful discussions with and preliminary work performed by Antony Orth and David Liu of the National Research Council Canada.

Disclosures. The authors declare no conflicts of interest.

Data availability. Data underlying the results presented here are available upon reasonable request.

Supplemental document. See Supplement 1 for supporting content.

References

1. J.-X. Cheng and X. S. Xie, eds., *Coherent Raman Scattering Microscopy* (CRC Press, 2016).
2. R. C. Prince, R. R. Frontiera, and E. O. Potma, "Stimulated Raman Scattering: From Bulk to Nano," Chem. Rev. **117**(7), 5070–5094 (2017).
3. Q. Cheng, Y. Miao, J. Wild, *et al.*, "Emerging applications of stimulated Raman scattering microscopy in materials science," Matter **4**(5), 1460–1483 (2021).
4. Y. Li, B. Shen, S. Li, *et al.*, "Review of Stimulated Raman Scattering Microscopy Techniques and Applications in the Biosciences," Adv. Biol. **5**(1), 2000184 (2021).
5. J.-X. Cheng, W. Min, Y. Ozeki, *et al.*, eds., *Stimulated Raman Scattering Microscopy* (Elsevier, 2022).
6. F. S. Pavone and P. J. Campagnola, eds., *Second Harmonic Generation Imaging* (CRC Press, 2016).
7. D. Fu, T. Ye, T. E. Matthews, *et al.*, "Probing skin pigmentation changes with transient absorption imaging of eumelanin and pheomelanin," J. Biomed. Opt. **13**(5), 054036 (2008).
8. M. C. Fischer, J. W. Wilson, F. E. Robles, *et al.*, "Invited Review Article: Pump-probe microscopy," Rev. Sci. Instrum. **87**(3), 031101 (2016).
9. Y. Zhou, D. Grass, W. S. Warren, *et al.*, "Non-destructive three-dimensional imaging of artificially degraded CdS paints by pump-probe microscopy," J. Phys. Photonics **6**(2), 025013 (2024).
10. A. D. Slepkov, A. Ridsdale, H.-N. Wan, *et al.*, "Forward-collected simultaneous fluorescence lifetime imaging and coherent anti-Stokes Raman scattering microscopy," J. Biomed. Opt. **16**(2), 021103 (2011).
11. J. Moger, N. L. Garrett, D. Begley, *et al.*, "Imaging cortical vasculature with stimulated Raman scattering and two-photon photothermal lensing microscopy," J. Raman Spectrosc. **43**(5), 668–674 (2012).
12. J. C. Mansfield, G. R. Littlejohn, M. P. Seymour, *et al.*, "Label-free Chemically Specific Imaging in Planta with Stimulated Raman Scattering Microscopy," Anal. Chem. **85**(10), 5055–5063 (2013).
13. K. Duppen, F. de Haan, E. T. J. Nibbering, *et al.*, "Chirped four-wave mixing," Phys. Rev. A **47**(6), 5120–5137 (1993).
14. A. M. Zheltikov and A. N. Naumov, "High-resolution four-photon spectroscopy with chirped pulses," Quantum Electron. **30**(7), 606–610 (2000).
15. E. Gershgoren, R. A. Bartels, J. T. Fourkas, *et al.*, "Simplified setup for high-resolution spectroscopy that uses ultrashort pulses," Opt. Lett. **28**(5), 361 (2003).
16. T. Hellerer, A. M. Enejder, and A. Zumbusch, "Spectral focusing: High spectral resolution spectroscopy with broad-bandwidth laser pulses," Appl. Phys. Lett. **85**(1), 25–27 (2004).
17. D. Fu, G. Holtom, C. Freudiger, *et al.*, "Hyperspectral Imaging with Stimulated Raman Scattering by Chirped Femtosecond Lasers," J. Phys. Chem. B **117**(16), 4634–4640 (2013).
18. F. E. Robles, J. W. Wilson, M. C. Fischer, *et al.*, "Phasor analysis for nonlinear pump-probe microscopy," Opt. Express **20**(15), 17082 (2012).
19. M.-A. Houle, R. C. Burruss, A. Ridsdale, *et al.*, "Rapid 3D chemical-specific imaging of minerals using stimulated Raman scattering microscopy," J. Raman Spectrosc. **48**(5), 726–735 (2017).
20. L. Marcu, "Fluorescence Lifetime Techniques in Medical Applications," Ann. Biomed. Eng. **40**(2), 304–331 (2012).
21. W. Becker, ed., *Advanced Time-Correlated Single Photon Counting Applications*, vol. 111 of *Springer Series in Chemical Physics* (Springer International Publishing, Cham, 2015).
22. A. J. Walsh, J. T. Sharick, M. C. Skala, *et al.*, "Temporal binning of time-correlated single photon counting data improves exponential decay fits and imaging speed," Biomed. Opt. Express **7**(4), 1385 (2016).
23. R. Datta, T. M. Heaster, J. T. Sharick, *et al.*, "Fluorescence lifetime imaging microscopy: fundamentals and advances in instrumentation, analysis, and applications," J. Biomed. Opt. **25**(07), 1 (2020).
24. D. Xiao, N. Sapermsap, M. Safar, *et al.*, "On Synthetic Instrument Response Functions of Time-Correlated Single-Photon Counting Based Fluorescence Lifetime Imaging Analysis," Front. Phys. **9**, 635645 (2021).
25. P. Malý, D. Strachotová, A. Holoubek, *et al.*, "Interferometric excitation fluorescence lifetime imaging microscopy," Nat. Commun. **15**(1), 8019 (2024).
26. C. Dong, P. So, T. French, *et al.*, "Fluorescence lifetime imaging by asynchronous pump-probe microscopy," Biophys. J. **69**(6), 2234–2242 (1995).
27. C.-Y. Dong, C. Buehler, P. T. C. So, *et al.*, "Implementation of intensity-modulated laser diodes in time-resolved, pump–probe fluorescence microscopy," Appl. Opt. **40**(7), 1109 (2001).
28. J. R. Lakowicz, *Principles of Fluorescence Spectroscopy* (Springer US, Boston, MA, 2006), 3rd ed.
29. J. Miyazaki, K. Kawasumi, and T. Kobayashi, "Frequency domain approach for time-resolved pump-probe microscopy using intensity modulated laser diodes," Rev. Sci. Instrum. **85**(9), 093703 (2014).
30. J. W. Wilson, J. K. Park, W. S. Warren, *et al.*, "Flexible digital signal processing architecture for narrowband and spread-spectrum lock-in detection in multiphoton microscopy and time-resolved spectroscopy," Rev. Sci. Instrum. **86**(3), 033707 (2015).
31. S. E. Bialkowski, N. G. C. Astrath, and M. A. Proskurnin, *Photothermal Spectroscopy Methods* (Wiley, 2019).
32. D. G. Cahill, "Analysis of heat flow in layered structures for time-domain thermoreflectance," Rev. Sci. Instrum. **75**(12), 5119–5122 (2004).
33. J. P. Feser and D. G. Cahill, "Probing anisotropic heat transport using time-domain thermoreflectance with offset laser spots," Rev. Sci. Instrum. **83**(10), 104901 (2012).

34. J. P. Feser, J. Liu, and D. G. Cahill, “Pump-probe measurements of the thermal conductivity tensor for materials lacking in-plane symmetry,” Rev. Sci. Instrum. **85**(10), 104903 (2014).
35. O. Tzang, A. Pevzner, R. E. Marvel, *et al.*, “Super-Resolution in Label-Free Photomodulated Reflectivity,” Nano Lett. **15**(2), 1362–1367 (2015).
36. N. V. Chukanov and M. F. Vigasina, *Vibrational (Infrared and Raman) Spectra of Minerals and Related Compounds*, Springer Mineralogy (Springer International Publishing, Cham, 2020).
37. A. J. Schmidt, X. Chen, and G. Chen, “Pulse accumulation, radial heat conduction, and anisotropic thermal conductivity in pump-probe transient thermoreflectance,” Rev. Sci. Instrum. **79**(11), 114902 (2008).
38. J. T. Barron and B. Poole, “The Fast Bilateral Solver,” in *Computer Vision - ECCV 2016*, B. Leibe, J. Matas, N. Sebe, and M. Welling, eds., (Springer Cham, 2016), pp. 617–632.
39. P. D. Samolis and M. Y. Sander, “Phase-sensitive lock-in detection for high-contrast mid-infrared photothermal imaging with sub-diffraction limited resolution,” Opt. Express **27**(3), 2643 (2019).
40. P. D. Samolis, D. Langley, B. M. O’Reilly, *et al.*, “Label-free imaging of fibroblast membrane interfaces and protein signatures with vibrational infrared photothermal and phase signals,” Biomed. Opt. Express **12**(1), 303 (2021).
41. M. Andreana, M.-A. Houle, D. J. Moffatt, *et al.*, “Amplitude and polarization modulated hyperspectral Stimulated Raman Scattering Microscopy,” Opt. Express **23**(22), 28119 (2015).
42. S. Heuke, A. Lombardini, E. Büttner, *et al.*, “Simultaneous stimulated Raman gain and loss detection (SRGAL),” Opt. Express **28**(20), 29619 (2020).